Transitional Delayed Detached-Eddy Simulation for a Compressor Cascade

Möller, Felix M. ; Tucker, Paul G.; Wang, Zhong-Nan; Morsbach, Christian

DOI:
10.2514/1.B39344

Transitional Delayed Detached-Eddy Simulation for a Compressor Cascade: A Critical Assessment

Felix M. Möller*
German Aerospace Center (DLR), Cologne, 51147, Germany

Paul G. Tucker†
University of Cambridge, Cambridge, CB2 1PZ, United Kingdom

Zhong-Nan Wang‡
University of Birmingham, Birmingham, B15 2TT, United Kingdom

Christian Morsbach§
German Aerospace Center (DLR), Cologne, 51147, Germany

The accurate prediction of transitional flows is crucial for the industrial turbomachinery design process. While a Reynolds-averaged Navier-Stokes (RANS) approach inherently brings conceptual weaknesses, large-eddy simulation (LES) will be still too expensive in the near future to affordably analyze complex turbomachinery configurations. We introduce a transitional delayed detached-eddy simulation (DDES) model, namely DDES-γ, and analyze numerical results of the compressor cascade V103. A comparison with the fully turbulent DDES approach emphasizes the benefit of coupling DDES with a transition model. Issues with undesired decay of modelled turbulent kinetic energy in the free-stream are improved when running DDES-γ in combination with the synthetic turbulence generator method. Best results for DDES-γ are obtained when changing the inviscid flux solver blending from dynamic to constant mode. We show that DDES-γ is capable to predict the transitional flow through a linear compressor cascade, but also critically discuss the general concept and results.

Nomenclature

Greek symbols

γ	intermittency factor
δ_{ij}	Kronecker delta
Δ_{SLS}	sub-grid length scale, m
η	wall-normal distance, m

*Research Associate, Institute of Test and Simulation for Gas Turbines, felix.moeller@dlr.de (Corresponding Author)
†Rank Professor of Engineering, Department of Engineering
‡Lecturer (Assistant Professor) in Aerospace, College of Engineering and Physical Sciences
§Team Leader, Institute of Propulsion Technology
Presented as paper AIAA 2023-3421 at the AIAA AVIATION 2023 Forum in San Diego, CA, 12th-16th June 2023.

ζ	total pressure loss coefficient
κ	specific heat ratio
λ	thermal conductivity, $\mathrm{W \cdot m^{-1} \cdot K^{-1}}$
λ_t	turbulent conductivity, $\mathrm{W \cdot m^{-1} \cdot K^{-1}}$
μ	molecular viscosity, $\mathrm{N \cdot s \cdot m^{-2}}$
μ_t	eddy viscosity, $\mathrm{N \cdot s \cdot m^{-2}}$
ρ	density, $\mathrm{kg \cdot m^{-3}}$
σ_b	solver blending factor
τ_{ij}	viscous stress tensor, $\mathrm{N \cdot m^{-2}}$
ω	turbulent dissipation rate, $\mathrm{s^{-1}}$
Ω	vorticity magnitude, $\mathrm{s^{-1}}$

Latin symbols

c_{ax}	axial chord length, m
c_f	friction coefficient
c_p	pressure coefficient
c_P	heat capacity at constant pressure, $\mathrm{J \cdot kg^{-1} \cdot K^{-1}}$
c_V	heat capacity at constant volume, $\mathrm{J \cdot kg^{-1} \cdot K^{-1}}$
d	distance to the next viscous wall, m
e	internal energy, $\mathrm{m^2 \cdot s^{-2}}$
f_d	Spalart's shielding function
F_1, F_2	turbulence model blending functions
h	enthalpy, $\mathrm{m^2 \cdot s^{-2}}$
q_j	molecular heat flux vector, $\mathrm{kg \cdot s^{-3}}$
k	turbulent kinetic energy, $\mathrm{m^2 \cdot s^{-2}}$
l	length scale, m
N_g	number of mesh points
p	pressure, $\mathrm{N \cdot m^{-2}}$
P_k, D_k	production and destruction term k_{mod}, $\mathrm{kg \cdot m^{-1} \cdot s^{-3}}$
P_γ, D_γ	production and destruction term of γ, $\mathrm{kg \cdot m^{-3} \cdot s^{-1}}$
R	specific ideal gas constant, $\mathrm{J \cdot kg^{-1} \cdot K^{-1}}$
S_c	Sutherland constant, K
S_{ij}	strain rate tensor, $\mathrm{s^{-1}}$
t	time, s
t_c	convective time, s
T	temperature, K
u_i, u_j	velocity vector, $\mathrm{m \cdot s^{-1}}$
u_{tang}	tangential velocity, $\mathrm{m \cdot s^{-1}}$
x_i, x_j	coordinate vector, m

Subscripts

$\square_{\mathrm{mod}}$	modelled component
$\square_{\mathrm{res}}$	resolved component
$\square_{\mathrm{tot}}$	total component (modelled + resolved)
$\square_{\mathrm{tang}}$	tangential component
$\square_{\mathrm{ref}}$	reference component

I. Introduction

Covering laminar-to-turbulent transition with modern CFD methods is crucial for an accurate turbomachinery design process with the development of pure Reynolds-averaged Navier-Stokes (RANS) transition models still being an active field of research. Nevertheless, weaknesses coming from the RANS approach itself limit the predictive quality of steady RANS simulations. On the other hand, the large-eddy simulation (LES) method can be used to accurately predict the transition process (see e.g. Lardeau et al. [1], Marty [2] or Scillitoe et al. [3]). Since the computational effort of LES scales non-linearly with the Reynolds number, this method is too expensive to simulate realistic turbomachinery configurations on a day-to-day basis in an industrial design process. To combine the advantages from both approaches, seamless hybrid RANS/LES (HRL) methods have been introduced. They employ a RANS model in regions where RANS is capable of producing accurate results. In regions where RANS models fail, on the other

hand, HRL methods are meant to switch to an LES-mode to resolve turbulent scales and ensure high predictive quality. While the main focus of development has been on fully turbulent flows for the last decades, it is important to also be able to appropriately consider transitional flows, especially for turbomachinery applications. Hence, the prediction of transitional flows with HRL methods, such as delayed detached-eddy simulation (DDES), has recently received more attention.

To the author's knowledge, Magagnato et al. [4] were the first who presented an assessment of the original detached-eddy simulation (DES) model (Spalart et al. [5]) without an additional transition model for transitional flows in a VKI turbine cascade. Numerical results were '*less satisfactory*' [4], which can be seen as expectable when running a model designed for fully turbulent flows in transitional configuration. Wang et al. [6] first mentioned the potential of coupling a RANS transition model with the DES framework after they introduced a modular RANS transition model based on an additional transport equation for the intermittency factor γ. This model has been reworked in the HRL context [7] showing improved results and the capability of predicting transitional flows with the DDES model for the flow over a highly loaded Controlled Diffusion Airfoil (CDA). Xiao et al. [8] also proposed the coupling of the classical DDES model with a one-equation γ-transition model (introduced by Wang and Fu [9]) and computed the flow past the Orion capsule. Sørensen et al. [10] and Sa et al. [11] coupled a DES model with the two-equation γ-Re_θ transition model and showed improved results in the prediction transition over a circular cylinder, the DU-96-W-351 airfoil and the Eppler 387 airfoil. Alam et al. [12] proposed another concept based on the three-equation k-k_l-ω model by Walters et al. [13]. Their coupled model was able to predict the transition process on the surface of the PAK-B airfoil. Yin et al. [14] introduced a transitional DDES model based on the adaptive l^2-ω model demonstrating improved results for the ERCOFTAC T3 flat plate series and in another publication for the compressor cascade V103 [15]. This variety of different approaches illustrates both the importance of this research field and the need for further research as no definite concept has emerged yet.

Since the DDES model is mainly designed for massively separated flows, the most obvious transition type to consider is separation-induced transition. Therefore, we introduced a way to couple the DDES with the γ-transition model (DDES-γ) and presented an assessment of the model combination for separation-induced transition [16]. Besides separation-induced transition, Mayle [17] determines bypass transition and wake-induced transition as main types occurring in turbomachinery flows, while natural transition can be neglected due to increased free-stream turbulence intensity (FSTI). After assessing the model in cases featuring only separation-induced transition (cf. [16]), it is the next logical step, to consider cases including bypass transition. While wake-induced transition is important especially when simulating multi-row and multi-stage configurations, this will be focus of future work. To assess the coupled DDES-γ model, we chose the compressor cascade V103 which is a linear cascade based on the NACA-65 profile and features separation-induced transition on the suction side and bypass transition on the pressure side. In the following, we will discuss the concept of coupling the DDES model with the correlation-based γ-transition model. Before analyzing

physical results of the flow through the compressor cascade V103, the model itself and respective switches and functions will be discussed in Sec. II. These relations will help to judge computational results of the compressor cascade V103 in Sec. III. Finally, our results will be summarized in Sec. IV.

II. Methodology

A. Governing equations

To simulate unsteady, compressible flows, we solve the set of Favre-averaged Navier-Stokes equations numerically. In differential conservation form, the equations for mass, momentum and energy can be expressed as follows:

$$\frac{\partial \bar{\rho}}{\partial t} + \frac{\partial}{\partial x_i}\left(\bar{\rho}\tilde{u}_i\right) = 0 \tag{1}$$

$$\frac{\partial}{\partial t}\left(\bar{\rho}\tilde{u}_i\right) + \frac{\partial}{\partial x_j}\left(\bar{\rho}\tilde{u}_j\tilde{u}_i\right) = -\frac{\partial \bar{p}}{\partial x_i} + \frac{\partial}{\partial x_j}\left[\bar{\tau}_{ij} - \overline{\rho u_i'' u_j''}\right] \tag{2}$$

$$\frac{\partial}{\partial t}\left[\bar{\rho}\left(\tilde{e} + \frac{\tilde{u}_i\tilde{u}_i}{2}\right)\right] + \frac{\partial}{\partial x_j}\left[\tilde{u}_j\bar{\rho}\left(\tilde{h} + \frac{\tilde{u}_i\tilde{u}_i}{2}\right)\right] = \frac{\partial}{\partial x_j}\left[-\bar{q}_j - \bar{\rho}\widetilde{u_j'' h''}\right] + \frac{\partial}{\partial x_j}\left[\tilde{u}_i\left(\bar{\tau}_{ij} - \overline{\rho u_i'' u_j''}\right)\right] \tag{3}$$

where $\square''$ marks the fluctuating part of each component and $\overline{\square}$ and $\widetilde{\square}$ denote the Reynolds- and Favre-averaged value, respectively. The symbols ρ, u_i, p, τ_{ij}, e, h, q_j represent the density, velocity vector in cartesian coordinates, pressure, viscous stress tensor, internal energy, enthalpy and heat flux vector, respectively. The viscous stress tensor is defined as

$$\bar{\tau}_{ij} = 2\mu\left(\tilde{S}_{ij} - \frac{1}{3}\tilde{S}_{kk}\delta_{ij}\right) \tag{4}$$

with the molecular viscosity μ, the Kronecker delta operator δ_{ij} and the strain rate tensor

$$\tilde{S}_{ij} = \frac{1}{2}\left(\frac{\partial \tilde{u}_i}{\partial x_j} + \frac{\partial \tilde{u}_j}{\partial x_i}\right). \tag{5}$$

The molecular heat flux vector

$$\tilde{q}_j = -\lambda\frac{\partial \tilde{T}}{\partial x_j} \tag{6}$$

is given by a diffusion law with a constant Prandtl number of

$$Pr = \frac{c_P\mu}{\lambda} = 0.72 \tag{7}$$

where c_P is the specific heat at constant pressure and λ is the thermal conductivity. The turbulent transport of heat (in Eq. (3)) is modelled using an analogous gradient diffusion law:

$$\bar{\rho}\widetilde{u_j'' h''} = -\lambda_t \frac{\partial \tilde{T}}{\partial x_j}. \tag{8}$$

Equivalent to the molecular heat flux vector in Eq. (6), this expression is closed with the turbulent conductivity λ_t computed with the turbulent Prandtl number

$$Pr_t = \frac{c_P \mu_t}{\lambda_t} = 0.9. \tag{9}$$

The ideal caloric and thermal state equations read

$$\tilde{e} = c_V \tilde{T} \tag{10}$$

$$\bar{p} = \bar{\rho} R \tilde{T} \tag{11}$$

with the temperature $\tilde{T}$, the specific heat at constant volume c_V and the specific ideal gas constant $R = 287.06\,\mathrm{J \cdot kg^{-1} \cdot K^{-1}}$. The specific heat ratio for an ideal gas is set to $\kappa = 1.4$. Sutherland's law is used to determine the molecular viscosity

$$\mu = \mu_{\mathrm{ref}} \left(\frac{\tilde{T}}{T_{\mathrm{ref}}} \right)^{3/2} \frac{T_{\mathrm{ref}} + S_c}{\tilde{T} + S_c} \tag{12}$$

as a function of temperature $\tilde{T}$ with the constants $\mu_{\mathrm{ref}} = 1.716 \times 10^{-5}\,\mathrm{N \cdot s \cdot m^{-2}}$, $T_{\mathrm{ref}} = 273.15\,\mathrm{K}$ and $S_c = 110.4\,\mathrm{K}$. The only missing term required to close the set of equations is the Reynolds stress tensor $\overline{\rho u_i'' u_j''}$ introduced by the process of Favre-averaging. We use Boussinesq's approximation, which assumes a linear correlation between the Reynolds stress tensor and the strain rate tensor introducing a turbulent eddy viscosity μ_t

$$-\overline{\rho u_i'' u_j''} = \mu_t \left[\left(\frac{\partial \tilde{u}_i}{\partial x_j} + \frac{\partial \tilde{u}_j}{\partial x_i} \right) - \frac{2}{3} \frac{\partial \tilde{u}_k}{\partial x_k} \delta_{ij} \right] - \frac{2}{3} \bar{\rho} k_{\mathrm{mod}} \delta_{ij} \tag{13}$$

with the modelled turbulent kinetic energy k_{mod} and μ_t itself computed from the underlying turbulence model.

B. Turbulence and transition model

1. DDES model

To determine the required turbulent eddy viscosity μ_t, we employ the DDES model based on the two-equation Menter-SST turbulence model (see Spalart et al. [18] and Menter [19]). For this model, μ_t is determined by

$$\mu_t = \frac{\bar{\rho} a_1 k_{\text{mod}}}{\max\left(a_1 \omega, \Omega F_2\right)} \tag{14}$$

with $a_1 = 0.31$, the modelled turbulent kinetic energy (TKE) k_{mod}, the specific dissipation rate ω, the vorticity magnitude Ω and a model specific blending function F_2.

The two transport equations for k_{mod} and ω read as follows:

$$\frac{\partial}{\partial t}(\bar{\rho} k_{\text{mod}}) + \frac{\partial}{\partial x_j}(\bar{\rho}\tilde{u}_j k_{\text{mod}}) = P_{k,\text{mod}} - D_{k,\text{mod}} + \frac{\partial}{\partial x_j}\left[(\mu + \sigma_k \mu_t)\frac{\partial k_{\text{mod}}}{\partial x_j}\right] \tag{15}$$

$$\begin{aligned}\frac{\partial}{\partial t}(\bar{\rho}\omega) + \frac{\partial}{\partial x_j}(\bar{\rho}\tilde{u}_j \omega) = \alpha \frac{\bar{\rho} P_{k,\text{mod}}}{\mu_t} - \beta \bar{\rho}\omega^2 + \frac{\partial}{\partial x_j}\left((\mu + \sigma_\omega \mu_t)\frac{\partial \omega}{\partial x_j}\right) \\ + 2(1 - F_1)\bar{\rho}\sigma_{\omega 2}\frac{1}{\omega}\frac{\partial k_{\text{mod}}}{\partial x_j}\frac{\partial \omega}{\partial x_j}.\end{aligned} \tag{16}$$

Here, $\sigma_{\omega 2}$ is a specific model constant and F_1 is another model blending function, which is also used to derive the parameters σ_k, σ_ω, α and β. The 'hybridization' of any two-equation RANS turbulence model is realized by modifying the destruction term $D_{k,\text{mod}}$ in Eq. (15). It can be expressed as a function of a model-specific length scale

$$D_{k,\text{mod}} = \frac{\bar{\rho} k_{\text{mod}}^{3/2}}{l_{\text{DDES}}}, \tag{17}$$

which, for the DDES model, is defined as

$$l_{\text{DDES}} = l_{\text{RANS}} - f_d \max\left(0, l_{\text{RANS}} - C_{\text{DES}}\Delta_{\text{SLS}}\right). \tag{18}$$

The RANS length scale can be expressed by $l_{\text{RANS}} = \sqrt{k_{\text{mod}}}/(\beta_k \omega)$ with $\beta_k = 0.09$. Δ_{SLS} is the specific sub-grid length scale (SLS) and $C_{\text{DES}} = 0.65$ is the recommend model constant by Travin et al. [20]. To verify our implementation, we simulated the Decaying Isotropic Turbulence (DIT) test case and confirmed a proper calibration with this value. For $f_d = 0$ or $l_{\text{RANS}} < C_{\text{DES}}\Delta_{\text{SLS}}$, the DDES length scale reduces to the original RANS length scale yielding RANS model behavior. The boundary layer shielding function f_d was introduced by Spalart et al. [18] to prevent LES-mode in a boundary layer, where the resolution would in principle allow resolved scales but none are present due to the upstream RANS mode, as this would yield unphysical results due to modelled stress depletion (MSD) and grid-induced separation

(GIS) ([18], [21]). It is defined as

$$f_d = 1 - \tanh\left[(C_{d1} r_d)^{C_{d2}}\right], \tag{19}$$

where $C_{d2} = 3$ follows the original proposal of Spalart et al. [18] and $C_{d1} = 20$ is in alignment with the investigations of Gritskevich et al. [21], focusing on the coupling of DDES with the Menter-SST model. The parameter r_d is given by

$$r_d = \frac{\nu_t + \nu}{\sqrt{\tilde{u}_{i,j}\tilde{u}_{i,j}}\kappa^2 d^2} \tag{20}$$

with the kinematic eddy viscosity ν_t and the kinematic viscosity ν, the velocity gradient tensor $\tilde{u}_{i,j}$, the Kármán constant κ and the distance to the wall d. The shielding function f_d must be considered as an 'enabler' for the LES-mode. It actively shields regions of the domain and prevents the LES-mode ($f_d = 0$), but does not actually activate this mode. The LES-mode is only activated, if $l_{\mathrm{RANS}} > C_{\mathrm{DES}}\Delta_{\mathrm{SLS}}$ and $f_d \neq 0$.

The sub-grid length scale Δ_{SLS} was initially computed based on the mesh only by Spalart et al. [5]. More recent approaches (cf. [22], [23], [24]) improved this length scale and also incorporate flow physics, such as the vorticity vector. The simulations in the present paper are based on the extended, vorticity-based Δ_{SLA} (= **s**hear **l**ayer **a**daptive) by Shur et al. [25], which is defined as

$$\Delta_{\mathrm{SLA}} = \tilde{\Delta}_\omega F_{\mathrm{KH}}(< \mathrm{VTM} >). \tag{21}$$

The length scale $\tilde{\Delta}_\omega$ is computed using the original vorticity-based approach by Mockett et al. [24] and $F_{\mathrm{KH}}(< \mathrm{VTM} >)$ is a special limiting term to reduce the sub-grid length scale drastically in initial shear layers. This term returns values in the range between 0.1 and 1.0. Details can be found in [25], which also contains a comprehensive comparison with the original grid-based approach. A further analysis of different sub-grid length scale approaches for transitional flows is shown in [16]. In the following, we use $\Delta_{\mathrm{SLS}} = \Delta_{\mathrm{SLA}}$ [25].

To easily distinguish between RANS- and LES-mode, the length scale ratio

$$l_{\mathrm{ratio}} = \frac{l_{\mathrm{RANS}}}{l_{\mathrm{DDES}}} \tag{22}$$

is often used. In RANS regions, we have $l_{\mathrm{ratio}} = 1$, because Eq. (18) yields $l_{\mathrm{DDES}} = l_{\mathrm{RANS}}$, while $l_{\mathrm{ratio}} > 1$ in LES regions. Increasing l_{ratio} values express a stronger modification of the k-transport equation in terms of a stronger reduction of modelled TKE. Values of $l_{\mathrm{ratio}} < 0$ are not possible for the DDES model. This simple differentiation between RANS- and LES-mode will be critically discussed for transitional cases.

2. γ-transition model

The transition model to be coupled with the fully turbulent DDES model is the one-equation γ-transition model, introduced by Menter et al. [26]. The γ-transport equation is defined as follows:

$$\frac{\partial}{\partial t}(\bar{\rho}\gamma) + \frac{\partial}{\partial x_j}(\bar{\rho}\tilde{u}_j\gamma) = P_\gamma - D_\gamma + \frac{\partial}{\partial x_j}\left[\left(\mu + \frac{\mu_t}{\sigma_\gamma}\right)\frac{\partial \gamma}{\partial x_j}\right]. \tag{23}$$

Details about the single terms and how the second transport equation for Re_θ is reduced to a functional expression can be found in [26]. We opted for the one-equation transition model, because of the reduced computational effort compared to a two-equation transition model. Further, the reported Galilean invariant model formulation (cf. [26]) is seen as an additional strength in comparison with the widely-used γ-Re_θ transition model [27].

3. Coupled DDES-γ model

The coupling of the γ-transition model with the RANS Menter-SST model is described in detail in [26]. The intermittency γ from Eq. (23) is integrated into the original k-transport equation (cf. Eq. (15)), yielding

$$\frac{\partial}{\partial t}(\bar{\rho}k_{\text{mod}}) + \frac{\partial}{\partial x_j}(\bar{\rho}\tilde{u}_j k_{\text{mod}}) = P_{k,\text{mod,trans}} + \cancel{P_k^{\text{lim}}} - D_{k,\text{mod,trans}} + \frac{\partial}{\partial x_j}\left[(\mu + \sigma_k\mu_t)\frac{\partial k_{\text{mod}}}{\partial x_j}\right] \tag{24}$$

with $P_{k,\text{mod,trans}} = \gamma P_{k,\text{mod}}$ and $D_{k,\text{mod,trans}} = \max(0.1, \gamma)D_{k,\text{mod}}$. The additional production term P_k^{lim} was intended for RANS simulations to accelerate the transition process in separated shear layers [26], but needs to be eliminated for a coupled DDES-γ model, as shown in [16]. Merging the destruction term of the fully turbulent DDES (cf. Eq. (17)) and the modified destruction term from the transition model coupling, we obtain

$$D_{k,\text{mod,trans}} = \max(0.1, \gamma)\frac{\bar{\rho}k_{\text{mod}}^{3/2}}{l_{\text{DDES}}}. \tag{25}$$

This redefined destruction term and setting $P_k^{\text{lim}} = 0$ in Eq. (24) build the foundation of the coupled DDES-γ model.

C. Numerical solver blending

For the fully turbulent DDES model, Travin et al. [20] proposed a *dynamic* solver blending factor σ_b which switches between a central and an upwind (cf. Roe [28]) formulation of the Riemann solver to compute the inviscid fluxes F_{inv}. The idea is to let the model control where to use the dissipative upwind flux F_{upwind} (desired in RANS/attached regions, to ensure a stable RANS-mode) and where to use a central flux F_{central} (desired in LES/separated regions, to facilitate the development of physical instabilities). The blending between these two formulations is realized with

$$F_{\text{inv}} = (1 - \sigma_b)F_{\text{central}} + \sigma_b F_{\text{upwind}}. \tag{26}$$

A detailed description of σ_b and its computation can be found in [20].

Another approach of 'blending' between inviscid central and upwind fluxes can be realized by a *constant* solver blending. It differs conceptually from the *dynamic* blending in that it defines a constant, user-defined fraction σ_b of upwind flux in each cell (cf. Eq. (26)). In Sec. III.B.3, we will discuss results for a *constant* solver blending and compare it to the *dynamic* blending approach.

D. Interaction of different model switches

After introducing all relevant model equations and parameters separately in the previous subsections, we discuss and illustrate their interaction theoretically, before interpreting numerical results. Relevant model parameters of DDES-γ are the RANS length scale l_{RANS}, sub-grid length scale Δ_{SLS}, shielding function f_d, intermittency factor γ and solver blending σ_b. The destruction term for our coupled DDES-γ model (cf. Eq. (25)) can be reformulated, so that the first four parameters are visible in a single term:

$$D_{k,\mathrm{mod,trans}} = \max(0.1,\gamma)\frac{\bar{\rho}k_{\mathrm{mod}}^{3/2}}{l_{\mathrm{RANS}} - f_d \max\left(0, l_{\mathrm{RANS}} - C_{\mathrm{DES}}\Delta_{\mathrm{SLS}}\right)}. \tag{27}$$

Based on this expression, the hierarchy of model values can be illustrated. Fig. 1 depicts schematics for a fully turbulent ($\gamma = 1$, Fig. 1a) and a transitional (Fig. 1b) model setup for the flow over a blade. In the initial RANS region of the fully turbulent model (①), modelled TKE is produced, leading to high values of k_{mod} prior to separation. At separation onset (②), a comparison of l_{RANS} and Δ_{SLS} is fair, since increased l_{RANS} values allow for the activation of LES-mode via the denominator in Eq. (27). The increased destruction term yields an active reduction of modelled TKE in this region. After reattachment, the model is designed to switch from LES- to RANS-mode (③). In short, the differentiation between RANS- and LES-mode for fully turbulent flows is sensible and easy to realize by comparing the respective length scales.

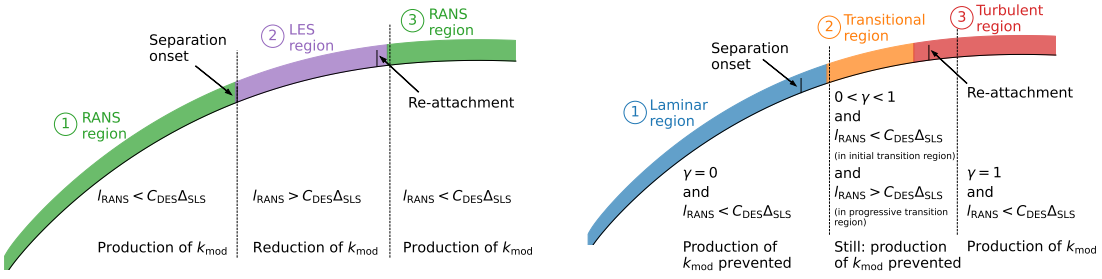

(a) Fully turbulent DDES **(b) Transitional DDES**

Fig. 1 Schematics of different model configurations and flow regions in streamwise direction.

The main difference between the fully turbulent and the transitional case is the state prior to separation. In contrast to the fully turbulent case, no significant k_{mod} is present in the transitional case. The clear classification of RANS and LES

regions is not possible anymore. For transitional cases, the model yields $\gamma = 0$ in the laminar region (Fig. 1b ①), which results in $P_{k,\mathrm{mod,trans}} = 0$ and $D_{k,\mathrm{mod,trans}}$ equal to 10 % of the original destruction. As a consequence, modelled TKE is kept to a minimum giving $l_{\mathrm{RANS}} \approx 0$. The usual comparison of l_{RANS} and Δ_{SLS} is no longer meaningful, since the 'LES-mode' ($l_{\mathrm{RANS}} > C_{\mathrm{DES}}\Delta_{\mathrm{SLS}}$) would only be possible on extremely fine meshes. For transitional cases, very small RANS length scales will always be smaller than a sub-grid length scale, resulting in a declaration of a RANS-mode, although it is more a laminar mode, where no turbulence is produced. Even in the transitional region (Fig. 1b ②), l_{RANS} is very small due to initially small values of γ, which inhibit the growth of the RANS length scale. After γ reaches unity, the original intention of the DDES model is restored and increasing modelled TKE is immediately reduced by the modified k-destruction term. In laminar regions, the DDES-γ acts more like an implicit LES model. The sub-grid (modelled) viscosity is kept to a minimum and the model attempts to resolve turbulent scales, which explains the demand for higher mesh resolution. Finally, it has to be stressed that the *dynamic* solver blending was designed for fully turbulent conditions requiring a clear distinction between RANS- and LES-mode. These aspects need to be considered when discussing our numerical setup and results in Sec. III.

E. Synthetic inflow turbulence

We also conducted simulations with the synthetic turbulence generator (STG) method (cf. Sec. III.B.2 and Sec. III.B.3) proposed by Shur et al. [29]. This method has been implemented and validated in *TRACE*[*] by Morsbach and Franke [30]. Further analysis was done by Matha et al. [31]. We omit discussing the STG model in detail at this point, since this is not focus of our work. Detailed information about the numerical STG settings will be given in Sec. III.A.

F. Comment on basis validation for bypass transition

We analyzed the behavior of DDES-γ for separation-induced transition with canonical and turbomachinery test cases in [16]. Before we assess the compressor cascade in Sec. III, we considered the T3C5 flat plate case from ERCOFTAC database[†] to validate the behavior of DDES-γ for pure bypass transition with a canonical test case. The FSTI of the T3C5 case is comparable to the compressor cascade analyzed in the following section which is why we picked this special case. The DDES-γ model showed identical results in comparison with the respective RANS-γ formulation. This was expected (or rather desired) since in attached transitional boundary layers we do not expect improvements by DDES-γ (in its original model configuration) and the coupling does not worsen results. At this point, we resign to illustrate numerical results, because a comparison RANS-γ and DDES-γ revealed identical results for this simple case. In the following section, we assess how the DDES-γ model acts for bypass transition in a more complex configuration.

[*] TRACE User Guide

[†] ERCOFTAC database: Flat Plate Transitional Boundary Layers

III. Linear compressor cascade V103

After we introduced the DDES-γ model and discussed interactions and conceptual differences to fully turbulent modelling approaches in the previous section, we will now assess the DDES models in a transitional flow through a compressor cascade. This test case was investigated experimentally by Hilgenfeld and Pfitzner [32]. The operating conditions (Ma = 0.67 and Re = 450 000) would have been too challenging for a direct numerical simulation (DNS), which is why Zaki et al. [33] decided to scale this case. Their DNS simulation serves as a numerical reference to better assess the results of DDES-γ. In the following, we first introduce the numerical setup, before we analyze DDES results. Where data is available, we always put our results into relation to other research groups.

A. Numerical setup

We consider the scaled operating point also simulated by Zaki et al. [33]. The scaling results in an inflow Mach number of Ma = 0.1 and a Reynolds number of Re = 138 500, based on the axial chord length $c_{\mathrm{ax}} = 0.204\,\mathrm{m}$ and the bulk inflow velocity $\bar{u}_0$. Due to the reduced Mach number, we neglect compressibility effects, thus, consider the Reynolds-averaged components for the velocity and temperature in the following. Characteristic parameters of the cascade are summarized in Table 1. The span size of $0.1c_{\mathrm{ax}}$ is also used by other research groups. An analysis of the two-point correlation confirms, that the spanwise extent is sufficient to properly capture turbulent coherent structures, which is the case when uncorrelated time signals can be detected within the domain.

Table 1 Overview of considered operating point and geometrical parameters.

Flow parameters	
Reynolds number Re	138 500
Mach number Ma	0.1
Inflow turbulence intensity TI	3.25 %
Inflow angle	42°
Geometrical parameters	
Axial chord length c_{ax}	0.204 m
Pitch y	0.12036 m
Span h	$0.1c_{\mathrm{ax}}$

Fig. 2 illustrates the computational domain. At the inlet (at $x/c_{\mathrm{ax}} = -0.4$, marked with green vertical line), we prescribe a total pressure value of $\bar{p}_{t,0} = 31\,369.84\,\mathrm{Pa}$ and a total temperature of $\bar{T}_{t,0} = 300.6\,\mathrm{K}$. Further, we either prescribe modelled turbulence via TI = 3.25 % and the turbulent length scale $l_t = 0.003c_{\mathrm{ax}}$ or we utilize the STG for the prescription of resolved turbulence (this is always the case for illustrated LES results and for DDES computations, where labelled). Therefore, we extract a bulk state from the RANS precursor simulation and provide the velocity vector, density and static pressure for the STG to compute the inlet boundary condition for resolved turbulence. Additionally,

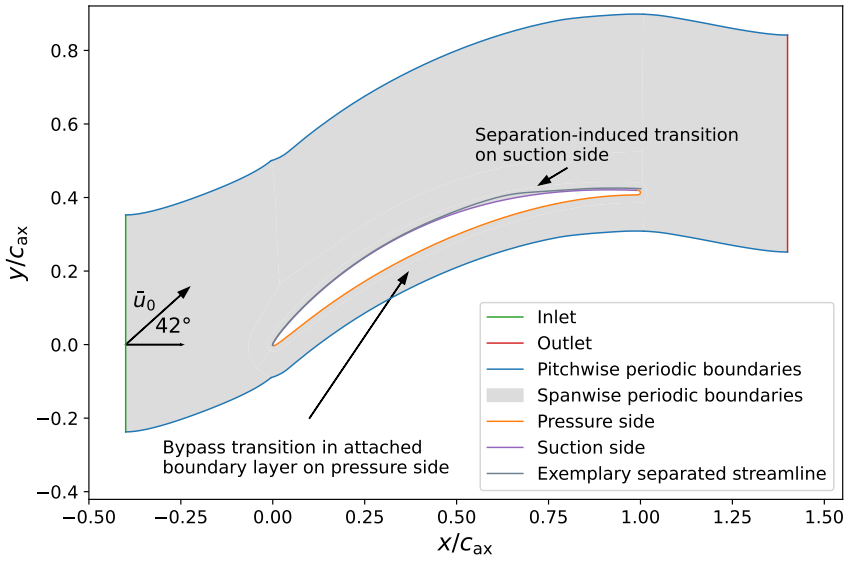

Fig. 2 Schematics of the numerical domain for the compressor cascade V103.

the length scale is increased to $l_t = 0.055 c_{ax}$. Differences in l_t for simulations without and with STG are explicable with the different definition of inflow boundary condition. For simulations with the STG, we follow the proposed inlet boundary condition of Shur et al. [29] where the inlet turbulent dissipation rate is defined as

$$\omega_{\text{inlet}} = \frac{\sqrt{k}}{\beta_k l_t} \tag{28}$$

with β_k as specific model constant, introduced in Sec. II.B. This constant is not used, when determining ω_{inlet} for simulations without the STG. To ensure a comparable inlet turbulent dissipation rate, we increase l_t for the STG simulation. At the outlet panel (at $x/c_{ax} = 1.4$, marked with red vertical line), we prescribe a constant static back pressure of $\bar{p}_{\text{out}} = 31\,240.65$ Pa, which was iteratively determined until the pressure distribution of the DNS reference data was met with acceptable accuracy. For the selected operating point (cf. Table 1) separation-induced transition can be found on the suction side. On the pressure side, bypass transition can be observed. The simultaneous appearance of two transition types is a challenging setup for the DDES-γ model, which motivates the assessment of this case.

To assess the sensitivity of the DDES setup, we considered three different mesh densities as summarized in Table 2. The spanwise resolution was kept constant at 40 cells for all simulations yielding equal non-dimensional cell sizes in spanwise direction Δz^+ for all simulations. A wall-normal resolution of $y^+ < 1$ is guaranteed for all setups. The integral total pressure loss ζ_{int} in the wake at $x/c_{ax} = 1.078$ is computed and compared to the one of the LES simulation. The pitchwise local total pressure loss is defined as

$$\zeta(y) = 1 - \frac{\bar{p}_t(y)}{\bar{p}_{t,0}} \tag{29}$$

Table 2 Mesh parameters of interest for varying mesh densities.

Simulation type	N_g	$\Delta x^+_{\text{max,ps}}$	$\Delta x^+_{\text{max,ss}}$	$\Delta z^+_{\text{max,ps}}$	$\Delta z^+_{\text{max,ss}}$
LES	10 859 760	11.67	11.29	28.51	31.29
DDES-coarse	675 720	43.60	36.89		
DDES-medium	1 079 440	35.66	31.02		
DDES-fine	4 317 760	16.73	15.61		

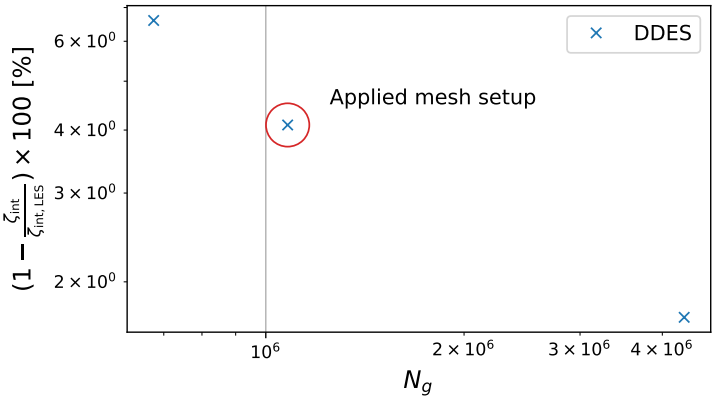

Fig. 3 Sensitivity study for varying mesh resolutions.

which is then integrated in pitchwise direction to obtain ζ_{int}. Fig. 3 shows the mesh dependence of the relative deviation of ζ_{int} from the LES. With finer mesh resolution, the DDES results converge towards the LES. We decided for the medium resolution, since this mesh is in close agreement with the one by Yin and Durbin [15]. Furthermore, a too fine mesh resolution reduces the motivation to apply DDES from a cost perspective. A visual impression of the selected mesh is given in Fig. 4. The DDES grid count, considered in the following, as well as the one for the LES are summarized in Table 3 and put in relation to other research groups who have simulated this case. The LES was conducted to obtain more detailed own reference data and uses the wall-adapting local eddy-viscosity (WALE) sub-grid model [34].

All simulations have been conducted with DLR's in-house solver *TRACE*[‡], which has been developed at the Institute of Propulsion Technology in the Department for Numerical Methods with special focus on turbomachinery applications. We employed the density-based cell-centered finite-volume solver of *TRACE*. The accuracy for the spatial discretization is of 2$^{\text{nd}}$-order with an additional inviscid flux blending, explained in Sec. II.C. The temporal discretization is realized with a 3$^{\text{rd}}$-order explicit Runge-Kutta method [35].

B. Results

In the following, we will assess the results of the coupled DDES-γ. All third-party references will be plotted using symbols (○). Own LES reference data is presented with a solid black line (—). The LES has been averaged for

[‡]TRACE User Guide

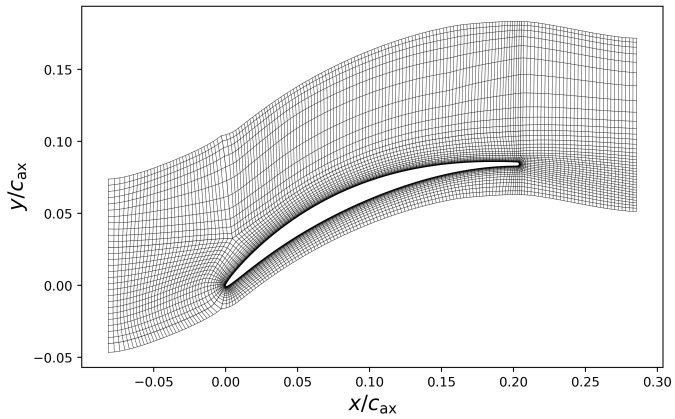

Fig. 4 Illustration of the blade-to-blade mesh in the x-y-plane for the medium mesh resolutions. Shown with every 2nd grid point.

Table 3 Overview of applied meshes and comparison to other research groups.

Simulation type	Authors	Total number of cells
DDES	Present paper	1 079 440
LES		10 859 760
DDES	Yin and Durbin [15]	1 474 560
LES	Lardeau et al. [1]	6 291 456
LES	Scillitoe et al. [3]	9 300 000
DNS	Zaki et al. [33]	83 886 080

$t/t_c = 11.5$ through flows, with the convective time of $t_c = c_{ax}/u_0$. For all DDES simulations, we ensure an averaging time of $t/t_c = 37$.

1. Comparison of baseline DDES-γ and DDES-FT

As a starting point, we consider the baseline DDES setup and compare results of the fully turbulent (FT) model with those of DDES-γ. This setup uses a *dynamic* solver blending and *no STG* and is more oriented towards a typical steady RANS setup. The main motivation for this comparison is to highlight differences between a transitional RANS, fully turbulent DDES and the transitional DDES-γ model.

We begin with the analysis of the pressure distribution c_p along the blade surface in Fig. 5 to verify the correct operation point. Besides our DDES results, we compare with DNS [33], RANS [26] and our own LES data. Generally, our LES and the DNS data show very good agreement. Evidently, RANS-γ is not capable of accurately predicting the separation bubble size on the suction side, while the deviations from the DNS data on the pressure side are not significant. The DDES-FT model fails to predict the separation bubble on the suction side and deviations on the pressure increase from $x/c_{ax} \approx 0.5$. Generally, the operating point deviates slightly as can be seen by the changed pressure level

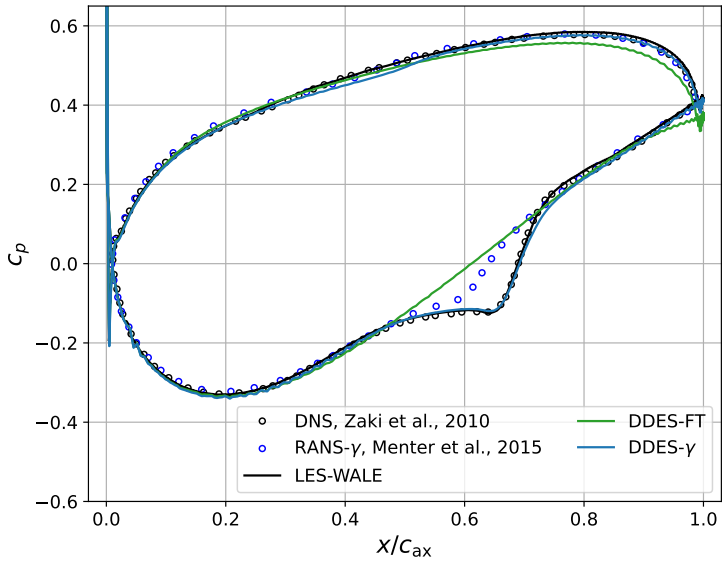

Fig. 5 Pressure distribution c_p along the blade surface.

at the trailing edge. On the other hand, the DDES-γbaseline setup already shows good agreement. The separation bubble on the suction side, as well as the pressure side distribution agree well with LES and DNS data.

Focusing on the suction side, we illustrate tangential velocity profiles prior to the separation in Fig. 6, revealing that DDES-FT quickly deviates from numerical reference data. The fully turbulent modelling approach yields prematurely increased modelled TKE in the boundary layer which does not represent the actual circumstances prior to the separation-induced transition. Our LES results are in very good agreement with the DNS reference data. The DDES-γ follows numerical references well, with acceptable deviations. For a better orientation, we show the boundary layer edge δ_{99} for the LES simulation in this plot as well as in the following boundary layer profile plots throughout the paper. This parameter is determined by the procedure described by Uranga et al. [36]. In separated regions, this approach is not capable to compute the boundary layer edge, which is why we set $\delta_{99} = 0$ in this case.

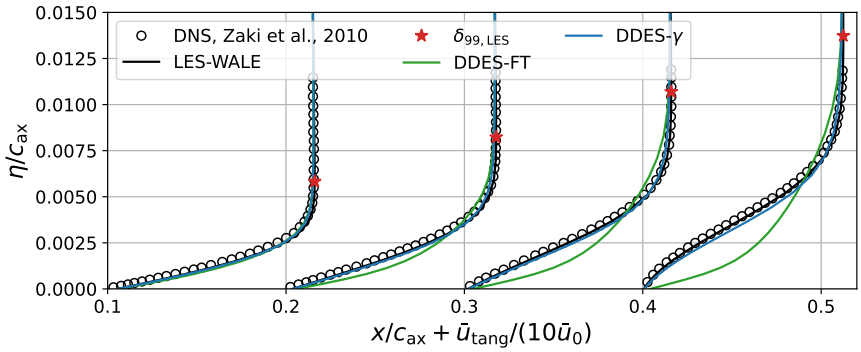

Fig. 6 Normalized tangential velocity profiles on the suction side prior to separation.

To further assess the transition processes on the blade surface, we consider the friction coefficient c_f in Fig. 7. In addition to the previously shown reference data, we also plot DDES data by Yin and Durbin [15]. Focusing on the suction side, in Fig. 7a, the positive trend is confirmed. While the fully turbulent DDES model does not capture the separation-induced transition process at all, DDES-γ shows reasonable agreement with the DNS reference data. Prior to separation and also prior to transition (at $x/c_{\mathrm{ax}} \approx 0.65$), DDES-$\gamma$ yields a friction coefficient almost identical to DNS. After transition and reattachment, we observe deviations which can be explained with the help of wall-normal TKE boundary layer cuts in Fig. 8. For DDES-FT we see, that the modelled TKE (Fig. 8a) is high in the wall vicinity

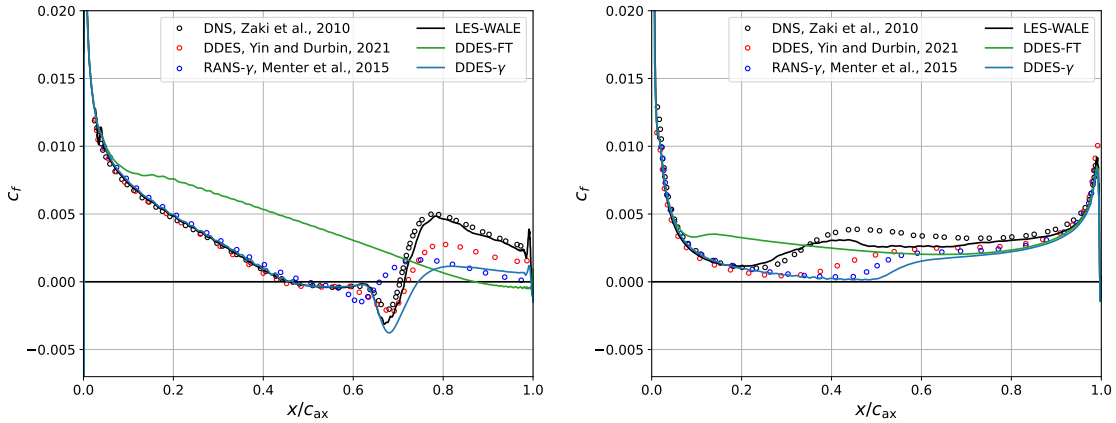

(a) Suction side **(b) Pressure side**

Fig. 7 Friction coefficient c_f along respective blade sides.

from the very first measurement station. Since for this simulation no STG was used, there is no resolved TKE for DDES-FT (cf. Fig. 8b). The premature production of k_{mod} suppresses the laminar separation bubble but leads to an open separation close to the trailing edge, which is why the DDES model does not switch to a resolved mode and modelled TKE is not reduced over the length of the blade. Overall, DDES-FT overpredicts the total level of TKE in the laminar region (cf. Fig. 8c) and lacks turbulence in the reattachment and turbulent region. For the DDES-γ model, the modelled TKE is kept to a minimum by the coupled γ-transition model in the laminar region ($x/c_{\mathrm{ax}} < 0.6$). Again, this simulation is conducted without the STG which is why resolved TKE is very low in the upstream stations of the suction side (cf. Fig. 8b between $0.1 \leq x/c_{\mathrm{ax}} \leq 0.5$). In the separation bubble (at $x/c_{\mathrm{ax}} = 0.6$), resolved content is in qualitative agreement with the LES. The low level of k_{mod} and the small gap of k_{res} between LES and DDES-γ after reattachment can explain the deviations in the friction coefficient in the reattachment region in Fig. 7a. The reduced turbulence levels in the boundary layer yield reduced momentum transfer which leads to a more laminar velocity profile close to the wall. This is why c_f is underestimated by DDES-γ in the reattachment region. To assess this, we illustrate γ-profiles for DDES-γ in the separated and post-reattachment region in Fig. 9. A reasonable production of modelled TKE is suppressed by the γ-model after the reattachment, especially in the region closest to the wall.

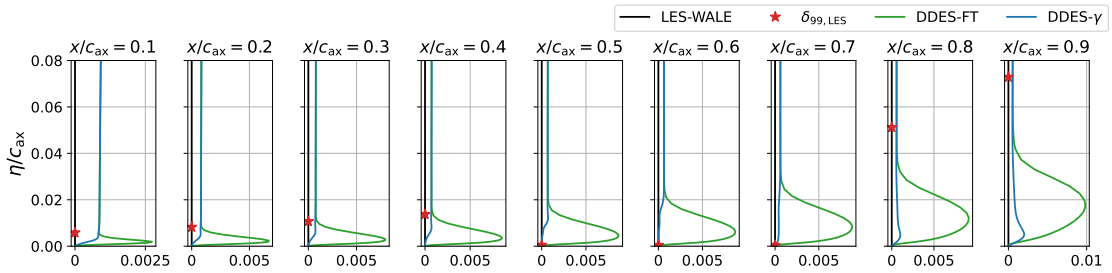

(a) Modelled turbulent kinetic energy $k_{\mathbf{mod}}/\bar{u}_0{}^2$

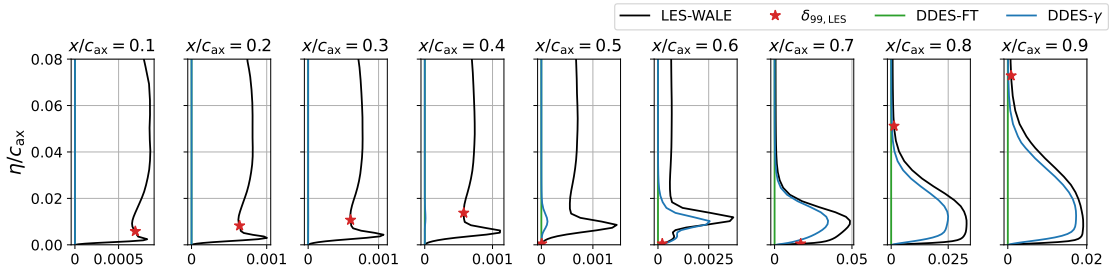

(b) Resolved turbulent kinetic energy $k_{\mathbf{res}}/\bar{u}_0{}^2$

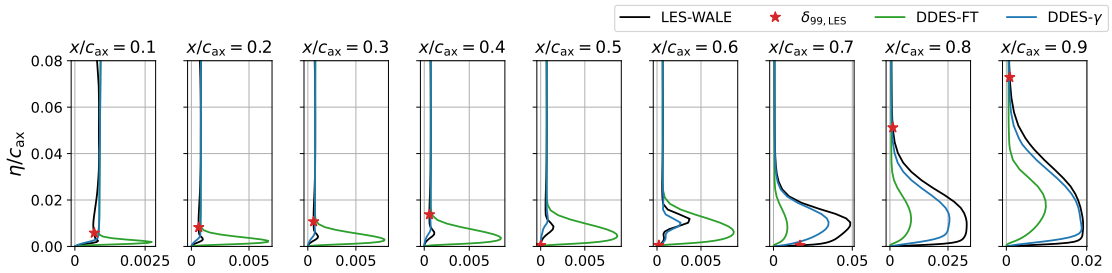

(c) Total turbulent kinetic energy $k_{\mathbf{tot}}/\bar{u}_0{}^2$

Fig. 8 Normalized wall-normal boundary layer cuts of the different TKE components along the suction side.

Coming back to the friction coefficient, we now focus on the pressure side in Fig. 7b. The fully turbulent approach DDES-FTis, by definition, not capable of predicting the bypass transition process. A missing transition model yields unphysical production of modelled TKE and premature 'transition' immediately downstream of the leading edge. For the bypass transition, DDES-γ results are more aligned with RANS-γ and do not follow the DNS reference data or DDES results of Yin and Durbin [15]. Massive improvements for the prediction of bypass transition compared to RANS-$\gamma$are not expected by the baseline setup, because the DDES model should behave as a RANS model in attached boundary layers.

To support this statement, we show boundary layer cuts of l_{ratio} and γ in Fig. 10. In Fig. 10a, it can be observed that the length scale ratio l_{ratio} rarely exceeds unity, which represents a constant RANS behavior on the blade pressure side. Without resolved content, we cannot expect any improvements of DDES-γ in comparison with RANS-γ. The minor deterioration by a slightly delayed transition onset can be explained when by the intermittency factor shown in Fig. 10b. In the outer boundary layer ($\eta/c_{\mathrm{ax}} > 0.1$), γ is equal to unity, which means that the underlying RANS model

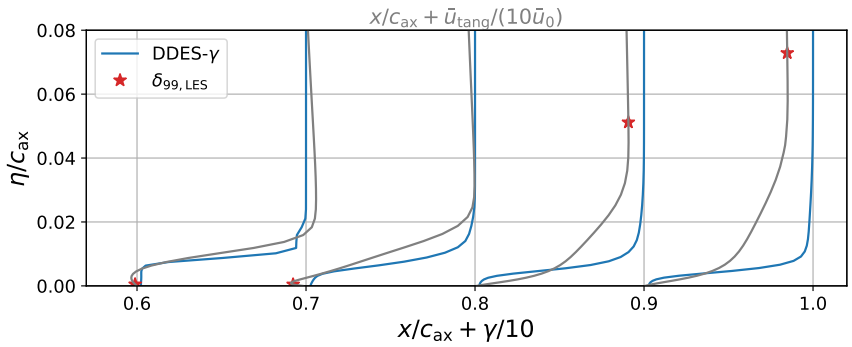

Fig. 9 Wall-normal intermittency profiles in the separated and post-reattachment region on the suction side.

is allowed to produce modelled TKEin this region. In contrast, the slight increase in length scale ratio recognizable between $0.4 \leq \eta/c_{ax} \leq 0.6$ means an undesired local reduction of the modelled TKE by the model which explains the missing modelled content to match the RANS-γ results for bypass transition.

The advantages of DDES-γ in comparison with DDES-FT has become clear throughout the previously presented results. Nevertheless, the baseline DDES-γ setup (*dynamic* solver blending and *no* STG) also revealed opportunities for further improvement. After explaining the minor deviations in the prediction of both transition types by the model behavior, we will now focus on the free-stream turbulence. Fig. 11 shows the total turbulence intensity along a streamline intersecting the leading edge plane at mid-pitch (illustrated by the dotted line). The modelled and resolved turbulence intensity components are not shown separately at this point, because no STG was used and for RANS and DDES

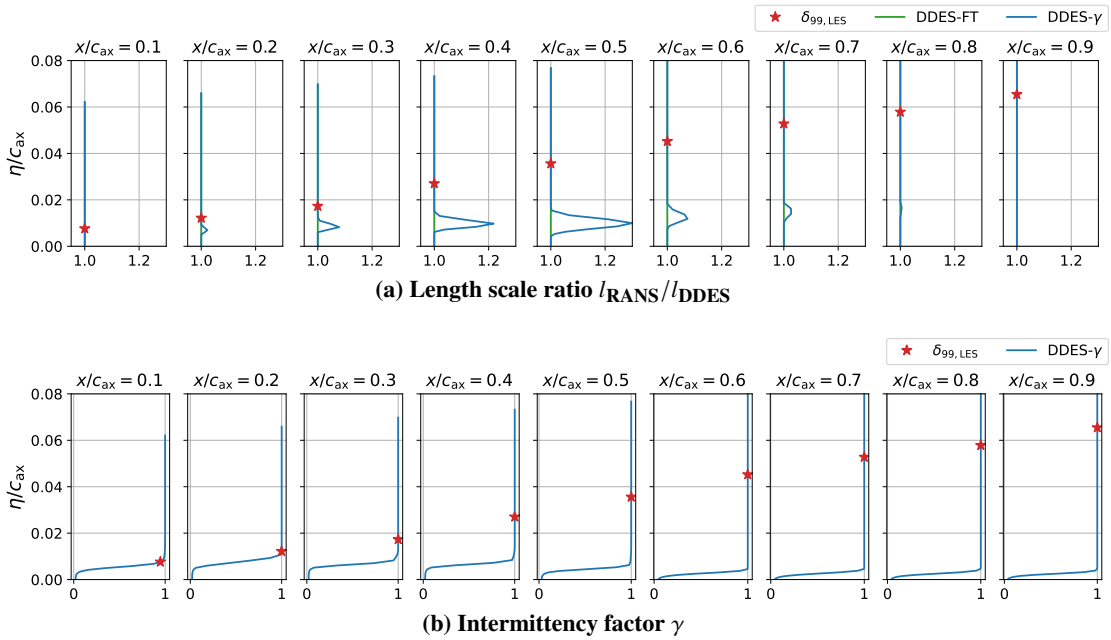

(a) Length scale ratio l_{RANS}/l_{DDES}

(b) Intermittency factor γ

Fig. 10 Wall-normal boundary layer cuts along the pressure side.

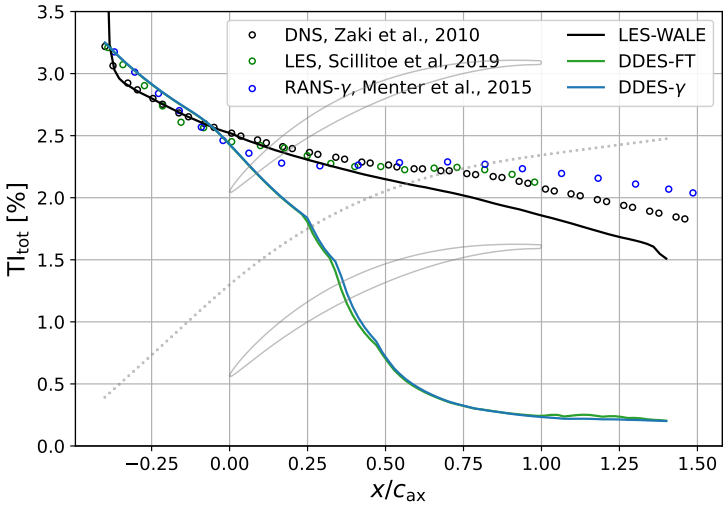

Fig. 11 Total turbulence intensity TI along extracted streamline intersecting the leading edge mid-pitch position.

simulations and, hence, the total turbulence intensity is equal to the modelled one. We illustrate the DNS reference data, but also LES results by Scillitoe et al. [3] and, again, RANS results. All these references and the conducted LES simulation follow the same trend. For both DDES results, another trend is can be observed. Close to the leading edge plane, the turbulence intensity decreases rapidly. This drop in FSTI is, in fact, unphysical and not desired. Without an STG, one would require the model to convect the modelled turbulence throughout the passage, as the RANS-γ model does.

An explanation for the strong decrease can be found in the shielding function f_d and the corresponding length scale ratio. We present exemplary 2D contour plots for DDES-γ in Fig. 12. Recalling the definition of l_{DDES} (see Eq. (18)) and physical meaning of l_{ratio} (see Eq. (22)), it becomes clear, that region of $f_d = 1$ in the free-stream in combination with high l_{ratio} values is the cause of the strong reduction of modelled TKE. The shielding function, spuriously, enables an LES-mode with $f_d = 1$ and the employed SLS approach by Shur et al. [25] determines very small Δ_{SLS}, which yield

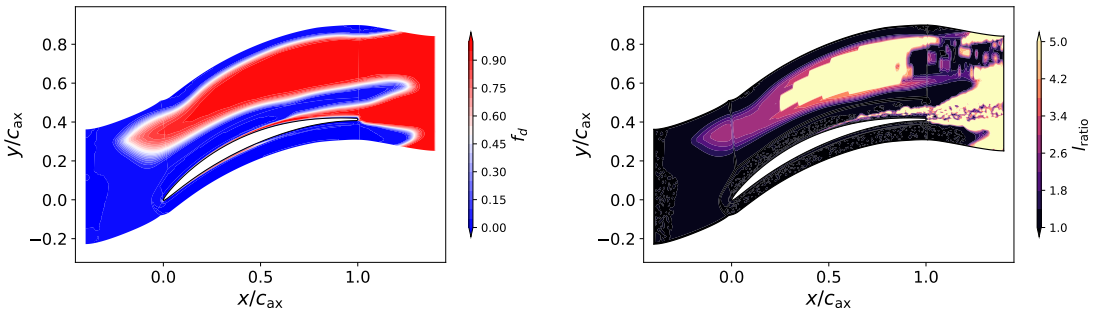

(a) Shielding function **(b) Length scale ratio**

Fig. 12 Time-averaged contour slices of spanwise-averaged variables for DDES-γ simulation.

a strong reduction of modelled TKE. Generally, this behavior is problematic if the gap in TKE is not filled with resolved scales in the free-stream, especially with the perspective of simulating multi-row or multi-stage configurations.

The presented results emphasize, that the coupled DDES-γ model is indeed superior to the original DDES-FT model. The combination with a transition model suppresses premature TKE and leads to improved transition prediction. Nonetheless, the baseline DDES setup (*dynamic* solver blending and *no* STG) does leave room for improvement such as predicting bypass transition and preserving modelled FSTI. In the following subsections, we will consider different setups and discuss their impact on DDES-γ simulations.

2. Assessment of the effect of STG for DDES-γ

After we analyzed the baseline DDES setup in the previous subsection and worked out differences between the fully turbulent and transitional approach, we now assess the impact of synthetic turbulence. Within this subsection, we run the DDES-γ model *without* and *with* STG, in the following referred to as DDES-γ and DDES-γ-STG, respectively. Still, the *dynamic* solver blending is used. Details about the STG setup can be found in Sec. III.A.

We start with the visualization of the friction coefficient c_f in Fig. 13. Focusing the suction side (Fig. 13a) first, the

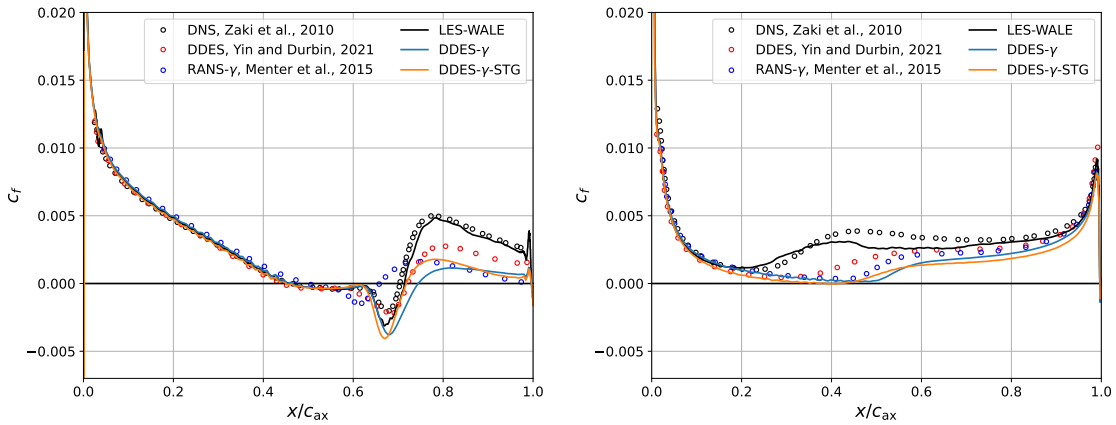

(a) Suction side **(b) Pressure side**

Fig. 13 Friction coefficient c_f along respective blade sides.

effect of STG is limited to the region of transition and reattachment. Small improvements in terms of a reattachment further upstream in agreement with the DNS and slightly increased c_f after reattachment can be observed. The surface values do not seem to be affected strongly by resolved scales in the free-stream. Fig. 14 shows boundary layer cuts of the resolved TKE on the suction side. The incoming resolved turbulence is apparent from the first station for DDES-γ-STG and in good agreement with our LES simulation, while DDES-γ does not determine any resolved content. Interestingly, the circumstances prior to separation are predicted almost identically by both approaches, as can be seen in the friction coefficient (Fig. 13a) and also with boundary layer velocity profiles (not shown here). At transition onset ($x/c_{ax} \approx 0.6$), both model approaches show a sudden increase of maximum resolved TKE. While DDES-γ-STG slightly

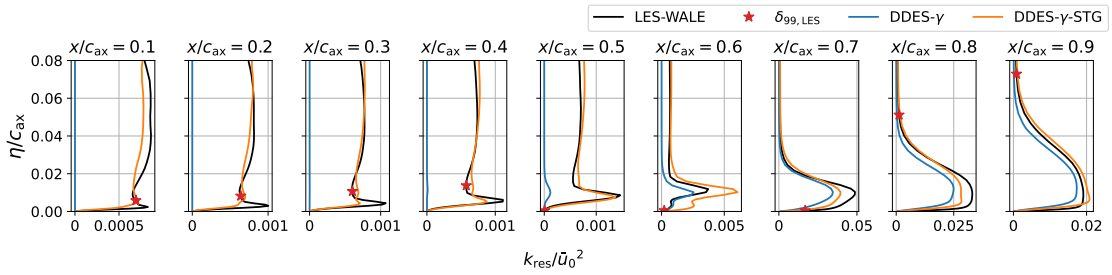

Fig. 14 Normalized wall-normal boundary layer cuts of resolved TKE along the suction side.

overpredicts k_{res}, DDES-γslightly underestimates the level of LES. The minor overprediction of resolved turbulence by DDES-γ-STG is the origin for the better agreement with LES results because the increased turbulence level yields an earlier closure of the separation bubble, as can be seen in Fig. 13a. Generally, using an STG is beneficial for the prediction of separation-induced transition in terms of c_f and k_{res} in comparison with our LES results.

The pressure side, as shown in Fig. 13b, requires further attention. For the bypass transition, the synthetic turbulence from the free-stream, shows no significant impact. The onset of transition is shifted slightly upstream towards other DDES or DNS reference. A potential reason for this lies in the DDES-γ model design. Note that assessing the transition process by surface values such as c_f only may lead to wrong conclusions. In the closest wall-vicinity, as can be seen in Fig. 15, the shielding function $f_d = 0$ enforces RANS-mode and, hence, prevents any resolution of turbulent scales. This is intended for the original DDES model concept, but for a simulation with an STG this behavior is potentially

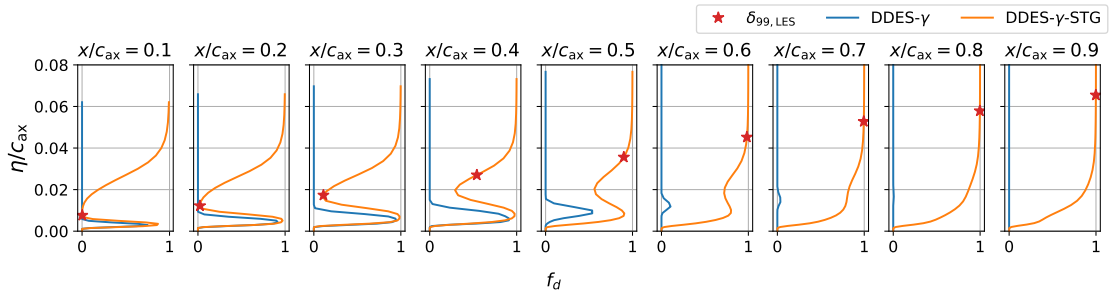

Fig. 15 Wall-normal boundary layer cuts of the shielding function along the pressure side.

not desired. If resolved scales are provided at the inflow, the mesh is most likely designed to be sufficiently fine in the wall-vicinity and, hence, a boundary layer shielding might not be required.

A more comprehensive assessment of the accurate prediction of the transition process on the pressure side is facilitated by the extraction of maximum modelled and resolved TKE for each streamwise boundary layer cut and plotting these values along the normalized x-axis. Results for the comparison of DDES-γ and DDES-γ-STG can be found in Fig. 16. Since the boundary layer cuts also consider the flow state away from the wall, a more complete picture of the transition process can be captured and the effect of the STG becomes more obvious. The simulation without

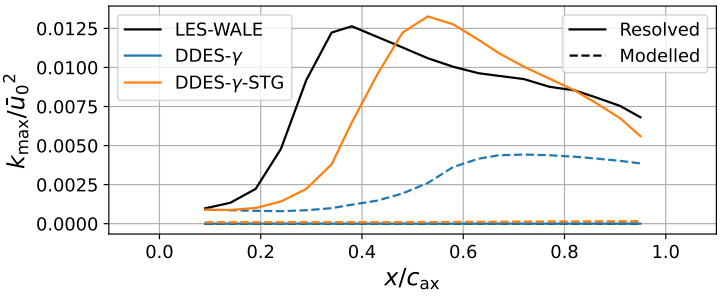

Fig. 16 Extracted maximum modelled and resolved TKE at streamwise boundary layer cuts on the pressure side.

resolved scales does not follow the trend of the LES and the transition process is predicted by modelled TKE, which can be seen in the increase of k_{mod} between $x = 0.5 - 0.65c_{ax}$. For DDES-γ-STG, bypass transition is now captured by resolved scales (see increase between $x = 0.3 - 0.55c_{ax}$), but shows a slight delay in comparison with the LES, which potentially has its origin in the coarser mesh resolution of the DDES simulation. The overall level of resolved TKE k_{res} is lower at the upstream stations, which yields this shift in Fig. 16.

The issue of unphysical decay of FSTI discussed above needs to be assessed for the STG setup, as well. The visualization of modelled, resolved and total TI in Fig. 17 confirms a positive impact of the STG on the FSTI. We already saw the strong decay of modelled, and thus, also total TKE for DDES-γ. For the simulation with STG, good agreement with DNS data is achieved by choosing appropriate values for TKE and length scale as input for the STG (Fig. 17b). The sum ($k_{mod} + k_{res}$) in Fig. 17c yields a slight overprediction, which we accept for this case. Since we now have resolved content in the free-stream, it is acceptable, that the shielding function f_d (see Fig. 18b) determines values equal to unity in the freestream. A reduction of modelled TKE is balanced by the resolved scales and even the modelled content is not reduced for DDES-γ-STG as can be seen in Fig. 17a. Fig. 17 and Fig. 18 show the positive effect of the STG on the prediction of the total FSTI and the proper working of the shielding function due to resolved turbulence, respectively.

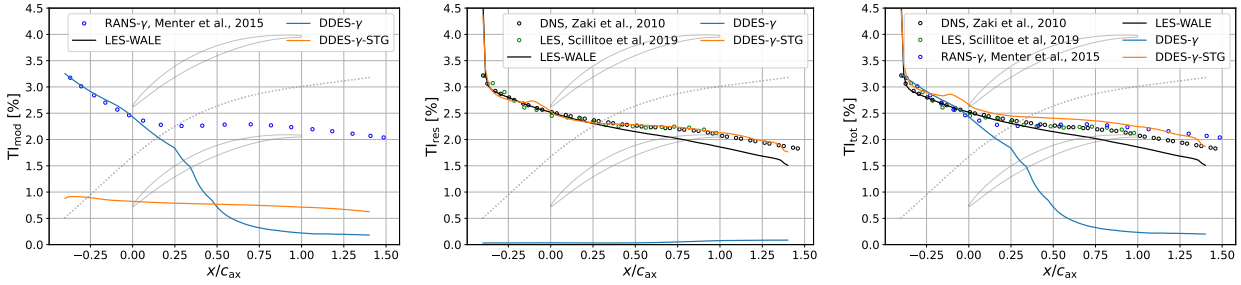

(a) Modelled component **(b) Resolved component** **(c) Modelled + resolved component**

Fig. 17 Turbulence intensity TI along extracted streamline intersecting the leading edge mid-pitch position.

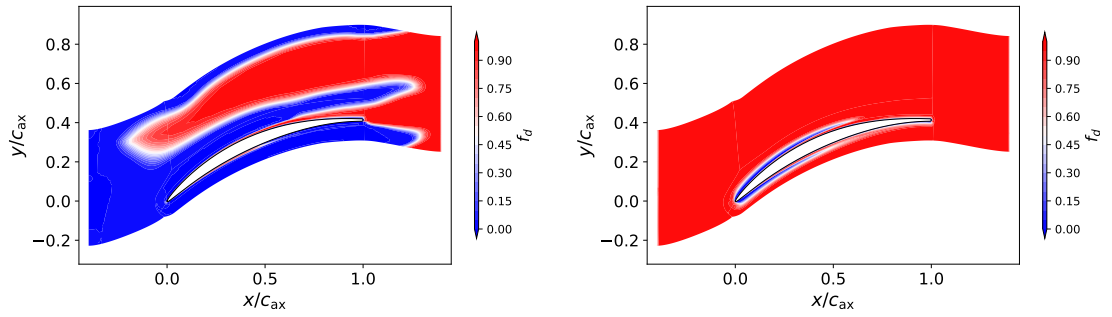

(a) DDES-γ **(b) DDES-γ-STG**

Fig. 18 Time-averaged contour slice of spanwise-averaged shielding function.

To sum up, when only focusing on surface values, the impact of resolved scales is small, even though the DDES-γ results *with* STG generally come closer to those of the DNS. A positive effect of an STG on the total turbulence level can be seen especially on the pressure side. Finally, the free-stream is handled more consistently, which means the prescribed turbulence is convected throughout the passage without unphysical decay.

3. Variation of inviscid flux blending for DDES-γ with STG

The results with DDES-γ and the STG shown above are promising but also show some deviations when focusing on the surface value c_f. In this subsection, we vary the numerical solver blending (described in Sec. II.C) with an active STG. Yin and Durbin [15] also applied a *constant* solver blending of 25 % upwind to avoid undesired numerical oscillations.

Before comparing the different solver blending results, we varied the amount of upwind as shown in Fig. 19. As expected, a 100 % central scheme yields oscillations by nature which are numerically undesired. The transitition process is not predicted correctly with the laminar separation on the suction side completely suppressed. An amount of 25 %, as used by [15], yields a stronger numerical damping which is undesired to maintain the resolved scales coming from the STG. The bypass transition is slightly shifted downstream and the separation bubble size is overpredicted. For the solver settings described in Sec. III.A, we eventually chose a constant upwind fraction of $\sigma_b = 5$ %. This value shows best agreement with DNS reference results. In the following, results of DDES-γ with *dynamic* solver blending labeled as DDES-γ-dyn are compared to results obtained with 5 % *constant* solver labelled as DDES-γ-const.

To illustrate the differences between *dynamic* and *constant* solver blending, we show boundary layer cuts of the blending factor in Fig. 20. While the *dynamic* approach derives the blending factor based on the flow physics and model specific parameters, the *constant* factor is simply visualized for orientation purposes. We learn, that on both blade sides, the *dynamic* blending approach produces a region of σ_b close to unity in the boundary layer, which marks a fully upwind region. This more dissipative solver scheme in the boundary layer has a direct impact on the physical results and affects the prediction of the transition processes negatively, because resolved scales from the STG are damped in the wall-vicinity. Fig. 21 confirms these findings. The separation-induced transition on the suction side (Fig. 21a)

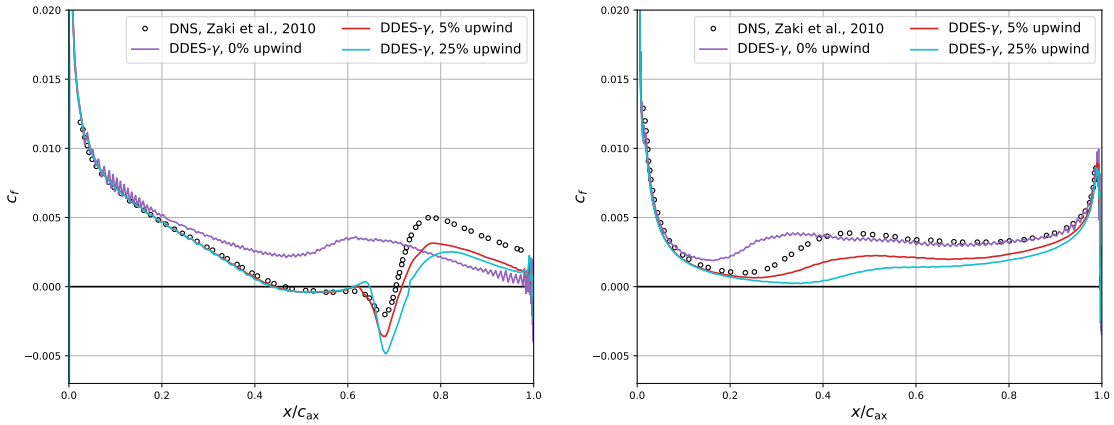

(a) Suction side **(b) Pressure side**

Fig. 19 Friction coefficient c_f along respective blade sides for varying fraction of upwind flux.

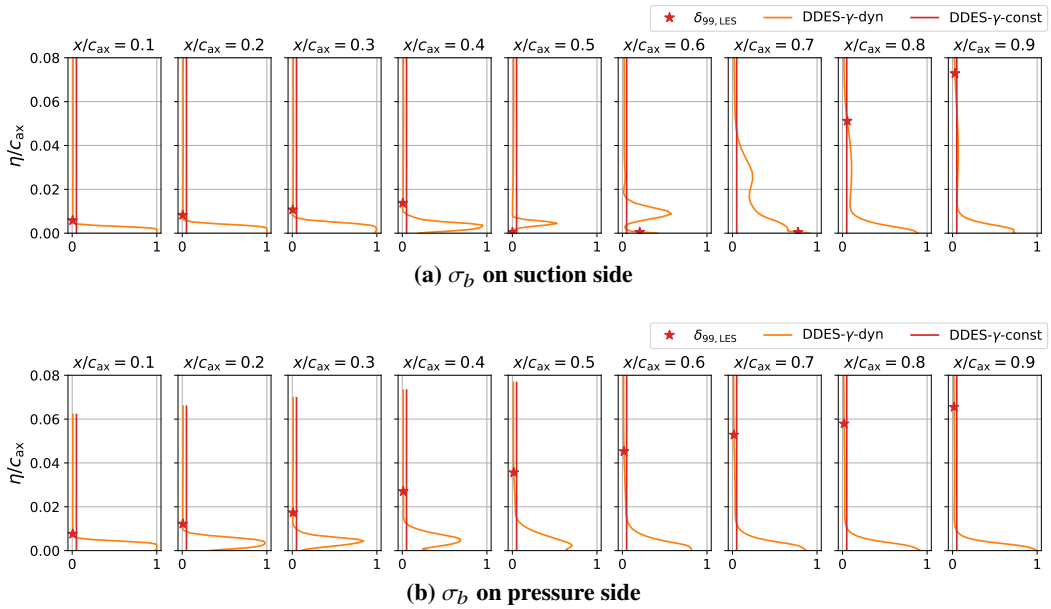

(a) σ_b on suction side

(b) σ_b on pressure side

Fig. 20 Boundary layer cuts of the solver blending factor on both blade sides separately.

and bypass transition on the pressure side (Fig. 21b) have been predicted more accurately by the DDES-γ-const. On both sides, we see good agreement with the DDES results of Yin and Durbin [15] and shift towards the DNS reference data. While DDES-γ-dyn deviates strongly from reference data, results with a *constant* solver blending are remarkably improved and closer to DNS reference data on the pressure side.

The effect of a higher upwind fraction in the boundary layer can be shown with k_{res} boundary layer cuts in Fig. 22. On the suction side in Fig. 22a small improvements by the *constant* blending approach are most evident at stations $0.4 \leq x/c_{\mathrm{ax}} \leq 0.7$, where results move closer to the LES data. The pressure side (Fig. 22b) shows larger differences between the two blending approaches. It becomes clear, that the results with *constant* solver blending follow the LES

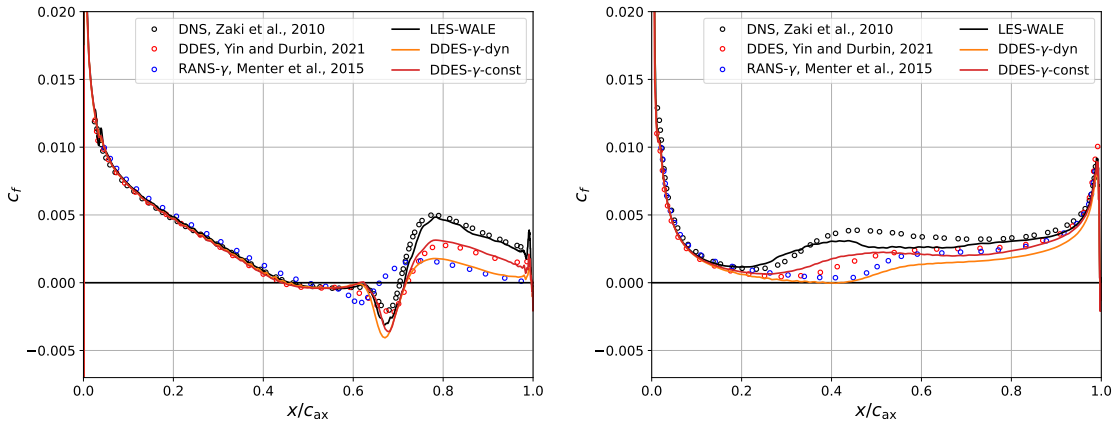

(a) Suction side **(b) Pressure side**

Fig. 21 Friction coefficient c_f along respective blade sides.

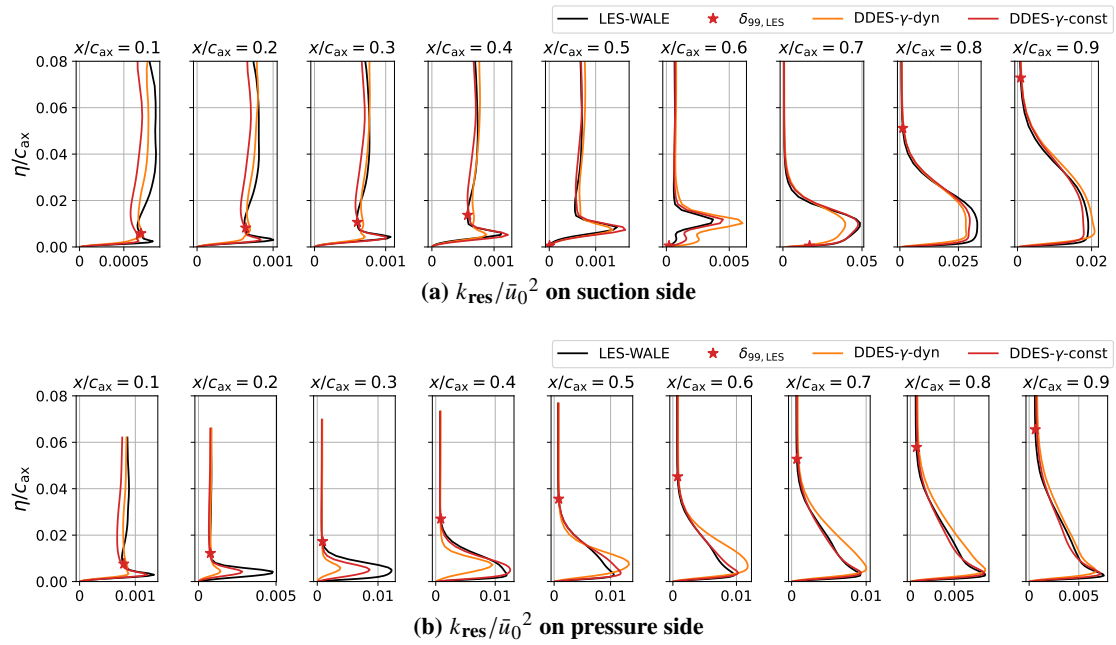

(a) $k_{res}/\bar{u}_0{}^2$ on suction side

(b) $k_{res}/\bar{u}_0{}^2$ on pressure side

Fig. 22 Boundary layer cuts of the normalized resolved TKE on both blade sides separately.

reference data even at upstream locations, whereas the *dynamic* approach underestimates resolved TKE. These results show the sensitivity of the transition process to the numerical dissipation, controlled by the solver blending *with* an active STG. We also varied the solver blending for setups *without* the STG (not shown in this work), but results were aligned with those of DDES-γ-dyn, which furthermore emphasizes the interdependency of resolved scales, coming from the STG, and the numerical dissipation, controlled by the solver blending approach.

A critical comment on this could be, that predicting the bypass transition process now relies on resolved turbulent scales. We obtain improved results with DDES-γ and the *constant* solver blending, but it is questionable if we are still

in the originally intended application range or if the model now acts more like an LES model. We already commented on this in the methodology section (cf. Sec. II.D). Moreover, the choice of the *constant* blending factor can be seen as another adjustable model parameter. We saw, that with the constant factor, the resolved turbulence is controlled and increased by less dissipation in the boundary layer. It cannot be said, that this factor will stand the test of time, because different test cases or rather modified mesh resolutions will yield other dissipative properties and the value of 5 % might have to be adjusted. Generally, the DDES-γ model with a *constant* solver blending shows improved results and reference data is met with acceptable accuracy.

IV. Conclusion and outlook

We gave an overview of the recently published transitional DDES approaches and motivated why this topic is relevant for the turbomachinery design process. After introducing our coupled DDES-γ model and discussing the model's behavior theoretically, its performance in a flow featuring both separation-induced and bypass transition was assessed with the compressor cascade V103. The main findings can be summarized as follows:

The comparison of baseline (*dynamic* solver blending and *no STG*) DDES-FT and DDES-γ illustrated the advantages of incorporating a transition model to predict transitional flows. While DDES-FT failed to predict both transition types, improvements could be shown for DDES-γ. The prediction of bypass transition with DDES-γ, on the other hand, does not improve compared to RANS-γ. We argued that this cannot be expected from a model approach which treats the attached boundary layer with RANS-mode and does not include any resolved content. As a weakness of DDES-γ, we found an unphysical decay of modelled FSTI for the baseline configuration.

With an STG at the inflow, however, the proper FSTI is maintained and in good agreement with reference data. Furthermore, the prediction of the separation-induced transition was improved, while deviations remain in the reattachment region. In terms of surface values, the prediction of bypass transition was only moderately improved, which could be explained with the model design. The shielding function f_d forces a RANS-mode in the closest wall-vicinity, which is why no significant impact of resolved scales on the friction coefficient c_f could be recognized. Assessing the transition process based on boundary layer cuts of the resolved TKE, beneficial behavior of DDES-γ-STG could be shown.

We finally compared *dynamic* and *constant* solver blending for the setup with an active STG. It could be seen, that the latter has a positive impact on the prediction of both transition types. The combination of resolved turbulence (STG) and a reduced amount of upwind fluxes in wall-vicinity allowed DDES-γ-const to capture the separation-induced transition and also remarkably improved the prediction of bypass transition.

The general strength of the DDES-γ could be illustrated and we showed, that an appropriate prediction of the transition processes on both blade side is possible. At the same time, we critically discussed the concept of DDES-γ and the obtained results. Future work will focus on more complex configurations, such as fully 3D compressor cascades and

multi-row/multi-stage setups. Especially for the latter, an assessment of the model in the presence of resolved turbulent wakes is required.

Acknowledgments

This research did not receive any specific grant from funding agencies in the public, commercial or non-for-profit sectors. All simulations have been carried out on DLR's supercomputer CARA[§] within the internal DLR project ADaMant[¶]. Eventually, we gratefully thank our colleagues at the Department, especially Michael Bergmann, Marcel Matha and Pierre Sivel, who spent a lot of time for discussions on this test case and the presented model.

References

[1] Lardeau, S., Leschziner, M., and Zaki, T., "Large Eddy Simulation of Transitional Separated Flow over a Flat Plate and a Compressor Blade," *Flow, Turbulence and Combustion*, Vol. 88, No. 1-2, 2011, pp. 19–44. https://doi.org/10.1007/s10494-011-9353-0.

[2] Marty, J., "Numerical Investigations of Separation-Induced Transition on High-Lift Low-Pressure Turbine Using RANS and LES Methods," *Proceedings of the Institution of Mechanical Engineers, Part A: Journal of Power and Energy*, Vol. 228, No. 8, 2014, pp. 924–952. https://doi.org/10.1177/0957650914548741.

[3] Scillitoe, A. D., Tucker, P. G., and Adami, P., "Large Eddy Simulation of Boundary Layer Transition Mechanisms in a Gas-Turbine Compressor Cascade," *Journal of Turbomachinery*, Vol. 141, No. 6, 2019, p. 061008. https://doi.org/10.1115/1.4042023.

[4] Magagnato, F., Pritz, B., and Gabi, M., "Comparison of DES and LES on the Transitional Flow of Turbine Blades," *Advances in Hybrid RANS-LES Modelling. Notes on Numerical Fluid Mechanics and Multidisciplinary Design*, Vol. 97, edited by S.-H. Peng and W. Haase, Springer Berlin Heidelberg, 2008, pp. 212–221. https://doi.org/10.1007/978-3-540-77815-8_22.

[5] Spalart, P., Jou, W.-H., Strelets, M., and Allmaras, S., "Comments on the Feasability of LES for Wings, and on a Hybrid RANS/LES Approach," *Advances in DNS/LES: Direct Numerical Simulation and Large Eddy Simulation*, Greyden Press, 1997, pp. 137–148.

[6] Wang, L., Fu, S., Carnarius, A., Mockett, C., and Thiele, F., "A Modular RANS Approach for Modelling Laminar–Turbulent Transition in Turbomachinery Flows," *International Journal of Heat and Fluid Flow*, Vol. 34, 2012, pp. 62–69. https://doi.org/10.1016/j.ijheatfluidflow.2012.01.008.

[7] Wang, L., Mockett, C., Fu, S., and Thiele, F., "Turbomachinery Flow Simulations Using a Hybrid RANS/LES Method Combined with a RANS Transition Model," *Proceedings XXI International Symposium on Air Breathing Engines: ISABE Conference Busan, Korea*, Vol. 2, American Institute for Aeronautics and Astronautics (AIAA), 2013, pp. 1040–1048.

[§]Link to technical specifications
[¶]Link to project homepage

[8] Xiao, Z., Wang, G., Yang, M., and Chen, L., "Numerical Investigations of Hypersonic Transition and Massive Separation past Orion Capsule by DDES-Tr," *International Journal of Heat and Mass Transfer*, Vol. 137, 2019, pp. 90–107. https://doi.org/10.1016/j.ijheatmasstransfer.2019.03.119.

[9] Wang, L., and Fu, S., "Modelling Flow Transition in a Hypersonic Boundary Layer with Reynolds-Averaged Navier-Stokes Approach," *Science in China Series G: Physics, Mechanics and Astronomy*, Vol. 52, No. 5, 2009, pp. 768–774. https://doi.org/10.1007/s11433-009-0047-8.

[10] Sørensen, N. N., Bechmann, A., and Zahle, F., "3D CFD Computations of Transitional Flows Using DES and a Correlation Based Transition Model," *Wind Energy*, Vol. 14, No. 1, 2011, pp. 77–90. https://doi.org/10.1002/we.404.

[11] Sa, J. H., Cho, K. W., and Park, S. H., "Numerical Study of Blending Hybrid RANS/LES Method and γ-Re_θ Transition Model for Unsteady Turbulent Flow Analysis," *The 2016 Structures Congress (Structures16)*, 2016. Jeju Island, Korea.

[12] Alam, M., Walters, D., and Thompson, D., "A Transition-Sensitive Hybrid RANS/LES Modeling Methodology for CFD Applications," *51st AIAA Aerospace Sciences Meeting including the New Horizons Forum and Aerospace Exposition*, 2013. https://doi.org/10.2514/6.2013-995, AIAA 2023-0995.

[13] Walters, D. K., Bhushan, S., Alam, M. F., and Thompson, D. S., "Investigation of a Dynamic Hybrid RANS/LES Modelling Methodology for Finite-Volume CFD Simulations," *Flow, Turbulence and Combustion*, Vol. 91, No. 3, 2013, pp. 643–667. https://doi.org/10.1007/s10494-013-9481-9.

[14] Yin, Z., Ge, X., and Durbin, P., "Adaptive Detached Eddy Simulation of Transition under the Influence of Free-Stream Turbulence and Pressure Gradient," *Journal of Fluid Mechanics*, Vol. 915, 2021, p. A115. https://doi.org/10.1017/jfm.2021.117.

[15] Yin, Z., and Durbin, P. A., "Detached Eddy Simulation of Transition in Turbomachinery: Linear Compressor Cascade," *Journal of Turbomachinery*, Vol. 144, No. 3, 2021, p. 031002. https://doi.org/10.1115/1.4052309.

[16] Möller, F., Tucker, P. G., Wang, Z.-N., Morsbach, C., and Bergmann, M., "On the Prediction of Separation-Induced Transition by Coupling Delayed Detached-Eddy Simulation with γ-Transition Model," *15th European Conference on Turbomachinery Fluid Dynamics and Thermodynamics*, European Turbomachinery Society, 2023. https://doi.org/10.29008/etc2023-375.

[17] Mayle, R. E., "The Role of Laminar-Turbulent Transition in Gas Turbine Engines," *Journal of Turbomachinery*, Vol. 113, No. 4, 1991, pp. 509–536. https://doi.org/10.1115/1.2929110.

[18] Spalart, P. R., Deck, S., Shur, M. L., Squires, K. D., Strelets, M. K., and Travin, A., "A New Version of Detached-Eddy Simulation, Resistant to Ambiguous Grid Densities," *Theoretical and Computational Fluid Dynamics*, Vol. 20, No. 3, 2006, pp. 181–195. https://doi.org/10.1007/s00162-006-0015-0.

[19] Menter, F. R., "Two-Equation Eddy-Viscosity Turbulence Models for Engineering Applications," *AIAA Journal*, Vol. 32, No. 8, 1994, pp. 1598–1605. https://doi.org/10.2514/3.12149.

[20] Travin, A., Shur, M., Strelets, M., and Spalart, P. R., "Physical and Numerical Upgrades in the Detached-Eddy Simulation of Complex Turbulent Flows," *Advances in LES of Complex Flows. Fluid Mechanics and Its Applications*, Vol. 65, edited by R. Friedrich and W. Rodi, Springer Netherlands, 2002, pp. 239–254. https://doi.org/10.1007/0-306-48383-1_16.

[21] Gritskevich, M. S., Garbaruk, A. V., Schütze, J., and Menter, F. R., "Development of DDES and IDDES Formulations for the k-ω Shear Stress Transport Model," *Flow, Turbulence and Combustion*, Vol. 88, No. 3, 2011, pp. 431–449. https://doi.org/10.1007/s10494-011-9378-4.

[22] Chauvet, N., Deck, S., and Jacquin, L., "Zonal Detached Eddy Simulation of a Controlled Propulsive Jet," *AIAA Journal*, Vol. 45, No. 10, 2007, pp. 2458–2473. https://doi.org/10.2514/1.28562.

[23] Probst, A., and Reuß, S., "Progress in Scale-Resolving Simulations with the DLR-TAU Code," *Deutscher Luft- und Raumfahrtkongress*, 2016.

[24] Mockett, C., Fuchs, M., Garbaruk, A., Shur, M., Spalart, P., Strelets, M., Thiele, F., and Travin, A., "Two Non-Zonal Approaches to Accelerate RANS to LES Transition of Free Shear Layers in DES," *Progress in Hybrid RANS-LES Modelling. Notes on Numerical Fluid Mechanics and Multidisciplinary Design*, Vol. 130, edited by S. Girimaji, W. Haase, S. Peng, and D. Schwamborn, Springer International Publishing, 2015, pp. 187–201. https://doi.org/10.1007/978-3-319-15141-0_15.

[25] Shur, M. L., Spalart, P. R., Strelets, M. K., and Travin, A. K., "An Enhanced Version of DES with Rapid Transition from RANS to LES in Separated Flows," *Flow, Turbulence and Combustion*, Vol. 95, No. 4, 2015, pp. 709–737. https://doi.org/10.1007/s10494-015-9618-0.

[26] Menter, F. R., Smirnov, P. E., Liu, T., and Avancha, R., "A One-Equation Local Correlation-Based Transition Model," *Flow, Turbulence and Combustion*, Vol. 95, No. 4, 2015, pp. 583–619. https://doi.org/10.1007/s10494-015-9622-4.

[27] Langtry, R. B., and Menter, F. R., "Correlation-Based Transition Modeling for Unstructured Parallelized Computational Fluid Dynamics Codes," *AIAA Journal*, Vol. 47, No. 12, 2009, pp. 2894–2906. https://doi.org/10.2514/1.42362.

[28] Roe, P., "Approximate Riemann Solvers, Parameter Vectors, and Difference Schemes," *Journal of Computational Physics*, Vol. 43, No. 2, 1981, pp. 357–372. https://doi.org/10.1016/0021-9991(81)90128-5.

[29] Shur, M. L., Spalart, P. R., Strelets, M. K., and Travin, A. K., "Synthetic Turbulence Generators for RANS-LES Interfaces in Zonal Simulations of Aerodynamic and Aeroacoustic Problems," *Flow, Turbulence and Combustion*, Vol. 93, No. 1, 2014, pp. 63–92. https://doi.org/10.1007/s10494-014-9534-8.

[30] Morsbach, C., and Franke, M., "Analysis of a Synthetic Turbulence Generation Method for Periodic Configurations," *ERCOFTAC Series*, Springer, 2017.

[31] Matha, M., Morsbach, C., and Bergmann, M., "A Comparison of Methods for Introducing Synthetic Turbulence," *6th ECCOMAS European Conference on Computational Mechanics: Solids, Structures and Coupled Problems, ECCM 2018 and 7th European Conference on Computational Fluid Dynamics, ECFD 2018*, 2018, pp. 278–289.

[32] Hilgenfeld, L., and Pfitzner, M., "Unsteady Boundary Layer Development Due to Wake Passing Effects on a Highly Loaded Linear Compressor Cascade," *Journal of Turbomachinery*, Vol. 126, No. 4, 2004, pp. 493–500. https://doi.org/10.1115/1.1791290.

[33] Zaki, T. A., Wissink, J. G., Rodi, W., and Durbin, P. A., "Direct Numerical Simulations of Transition in a Compressor Cascade: The Influence of Free-Stream Turbulence," *Journal of Fluid Mechanics*, Vol. 665, 2010, pp. 57–98. https://doi.org/10.1017/s0022112010003873.

[34] Nicoud, F., and Ducros, F., "Subgrid-Scale Stress Modelling Based on the Square of the Velocity Gradient Tensor," *Flow, Turbulence and Combustion*, Vol. 62, No. 3, 1999, pp. 183–200. https://doi.org/10.1023/a:1009995426001.

[35] Shu, C.-W., and Osher, S., "Efficient implementation of essentially non-oscillatory shock-capturing schemes," *Journal of Computational Physics*, Vol. 77, No. 2, 1988, pp. 439–471. https://doi.org/10.1016/0021-9991(88)90177-5.

[36] Uranga, A., Persson, P.-O., Drela, M., and Peraire, J., "Implicit Large Eddy Simulation of Transition to Turbulence at Low Reynolds Numbers Using a Discontinuous Galerkin Method," *International Journal for Numerical Methods in Engineering*, Vol. 87, No. 1-5, 2010, pp. 232–261. https://doi.org/10.1002/nme.3036.